RSC Advances

PAPER

View Article Online
View Journal | View Issue

Cite this: *RSC Adv.*, 2024, **14**, 1952

Synthesis of carbon dot based Schiff bases and selective anticancer activity in glioma cells†

Yafeng Zhuang,‡[a] Liping Zhu,‡[bc] Xiaoping Chen,‡[a] Jing Chen,[a] Zhoujie Ye,[bc] Jie Kang,*[a] Xinrui Wang*[bc] and Zhizhong Han *[a]

Schiff bases have remarkable anticancer activity and are used for glioma therapy. However, the poor water solubility/dispersibility limits their therapeutic potential in biological systems. To address this issue, carbon dots (CDs) have been utilized to enhance the dispersibility in water and biological efficacy of Schiff bases. The amino groups on the surface of CDs were conjugated effectively with the aldehyde group of terephthalaldehyde to form novel CD-based Schiff bases (CDSBs). The results of the MTT assays demonstrate that CDSBs have significant anticancer activity in glioma GL261 cells and U251 cells, with IC50 values of 17.9 μg mL^{-1} and 14.9 μg mL^{-1}, respectively. CDSBs have also been found to have good biocompatibility with normal glial cells. The production of reactive oxygen species (ROS) in GL261 glioma cells showed that CDSBs, at a concentration of 44 μg mL^{-1}, resulted in approximately 13 times higher intracellular ROS production than in the control group. These experiments offer evidence that CDSBs induce mitochondrial damage, leading to a reduction in mitochondrial membrane potential in GL261 cells. In particular, in this work, CDs serve not as carriers, but as an integral part of the anticancer drugs, which can expand the role of CDs in cancer treatment.

Received 20th September 2023
Accepted 2nd January 2024

DOI: 10.1039/d3ra06411e

rsc.li/rsc-advances

Introduction

The most prevalent primary tumor in the central nervous system is glioma, often observed in medical practice. Due to its low chance of cure and high death rate, it poses a serious hazard to human health.[1] The current common treatment approaches include surgery, radiotherapy, chemotherapy, *etc.* Temozolomide (TMZ) is the first-line clinical treatment for glioma, but the anticancer effect of TMZ is not ideal due to poor targeting, significant side effects, and a high resistance index.[2,3] Therefore, it is important to develop a new anticancer drug to improve the targeting effect of drugs and reduce toxic side effects.

A Schiff base is an organic compound that contains an imino group (–RC=N–), typically formed through the condensation reaction between an amine and an active carbonyl group. These compounds exhibit good anticancer, antioxidant, antibacterial, antifungal, and other biological activities, and have good application prospects in biological medicine.[4–8] For example, Nemat *et al.* prepared Schiff base derivatives of methotrexate to reduce the side effects of methotrexate and enhance the anticancer efficacy against glioma cells.[9] Chen *et al.* used *N*-phenylcarbazole (PhCz) triphenylamine to construct a Schiff base and further reacted with the dimers of iridium. Through a cytotoxicity test and a mechanism study, the results showed that the synthesized compound had a high anticancer effect (IC_{50}: 1.4–11.5 μM) with inhibition of metastasis and lysosomal damage.[10] However, most synthetic Schiff bases have the disadvantage of poor water solubility or dispersibility, which limits their biological applications. Scholars synthesized water-soluble Schiff bases by using more water-soluble substances as raw materials, such as glycylglycine,[11] hydrazine hydrate,[12] imidazole,[13] *etc.* The solubility or dispersibility of water was also increased by modifying polar groups to Schiff bases and by combining Schiff bases with metal ions to form ligand bonds with water.[14,15] For example, Chellan *et al.* obtained novel water-soluble Schiff base metal complexes ($[CuL(H_2O)_3]$) using glycylglycine and 4-nitrobenzaldehyde. Furthermore, the complexes showed well anticancer effects against HeLa (IC_{50}: 14 μg mL^{-1}) and HCT116 (IC_{50}: 10 μg mL^{-1}).[11] The synthesis of Schiff bases reported was usually performed in organic solvents. The process was complicated, requiring a long period of heating and stirring to synthesize the product and multiple purification steps, such as solvent removal, washing, and recrystallization.[11,14] In our study, the more water-dispersible carbon dots (CDs) work as raw materials for the synthesis of Schiff base. Therefore, the preparation process can be carried out in water.

[a]*School of Pharmacy, Fujian Medical University, Fuzhou, Fujian 350122, PR China. E-mail: zzhan@fjmu.edu.cn; davidkj660825@163.com*

[b]*Medical Research Center, Fujian Maternity and Child Health Hospital, College of Clinical Medicine for Obstetrics and Gynecology and Pediatrics, Fujian Medical University, Fuzhou 350011, Fujian, PR China. E-mail: wanxiru@sjtu.edu.cn*

[c]*NHC Key Laboratory of Technical Evaluation of Fertility Regulation for Non-Human Primate, Fujian Maternity and Child Health Hospital, Fuzhou 350011, Fujian, PR China*

† Electronic supplementary information (ESI) available. See DOI: https://doi.org/10.1039/d3ra06411e

‡ These authors contributed equally to this work.

CDs are light-emitting carbon nanomaterials. CDs are usually sphere-shaped structures, smaller than 10 nm in size, with a graphene-like core of hybridization of sp^2 and sp^3. The surface or edges of CDs are rich in various functional groups (such as carboxyl, amino, hydroxyl, *etc.*) or short chain polymer-like structures associated with carbon, oxygen, and nitrogen atoms.[16] This facilitates surface modification of CDs and their binding with other organic compounds. CDs have great potential in the field of biomedical applications because of their excellent biocompatibility, water dispersibility, cost-effectiveness, easy synthesis, and remarkable chemical stability properties.[17–20] They have found broad utilization in a variety of disciplines, including but not limited to bioimaging, drug delivery, and biosensing applications.[20–22] CDs used as drugs or drug carriers can improve water dispersibility of drugs, reduce the toxic side effects, enhance the efficacy without damaging normal cells.[23,24]

In this work, CDs with amine groups were synthesized using a straightforward one-step hydrothermal technique. The obtained CDs can be used for subsequent synthesis only by simple dialysis. Through the cytotoxicity test, we could see that CDs have good biocompatibility and low toxicity (IC_{50} > 300 μg mL^{-1}). The carbon dots-based Schiff bases (CDSBs) were successfully prepared from CDs and terephthalaldehyde (TPA) in aqueous solvent. As part of CDSBs, CDs not only increase the overall dispersibility of CDSBs in solution but also exert anticancer effects. Through the cytotoxicity test, we could know that CDSBs have a significant anticancer effect on GL261 cells at low concentration. Furthermore, the prepared CDSBs are less toxic to normal BV-2 cells. Therefore, CDSBs have better specificity for glioma cells and could better reduce their side effects.

Experimental section

Synthesis and characterization of CDs and CDs-based Schiff bases

0.84 g of citric acid (Macklin, China), 536 μL of polyethylene polyamine (Macklin, China) and 0.02 g of polyoxyethylene diamine (Macklin, China) were dissolved in 20 mL of hyperpure water, mixed well and reacted at 200 °C for 5 h. After be cooled to ambient temperature, the unreacted precursor was filtered through a 0.22 μm microporous membrane and dialyzed for 72 h in the dark using a 500–1000 Da dialysis bag. The purified CDs were then obtained and stored at 4 °C for use.

0.02 g of terephthalaldehyde (Macklin, China) was dissolved in 20 mL of ultrapure water at 55 °C, and then 4 mL of purified CDs (9.5 mg mL^{-1}) was added to the solution and reacted in the dark at 75 °C for 2.5 h to obtain CDSBs. We then used the vacuum freeze dryer (LC-10N-50A) to lyophilize CDSBs and calculated its usage concentration.

The morphology and structure of CDs and CDSBs were analyzed with transmission electron microscopy (TEM, FEI Talos F200s, USA). A Gensys 150 spectrophotometer (ThermoFisher Scientific, USA) was utilized to capture UV-Vis absorption spectra. The fluorescent spectra were taken by an F96PRO spectrofluorometer (Lengguang, China). The structures of CDs and CDSBs were characterised by Fourier transform infrared spectroscopy (Nicoletis50 infrared spectrometer, USA). X-ray photoelectron spectroscopy (XPS, K-Alpha+, ThermoFisher Scientific, USA) was used to analyze the surface structure and element state of the prepared samples. The source gun type of XPS was Al K_α and Lens Mode was standard mode. The analyzer mode of C, N and O was CAE: pass energy 30.0 eV and full spectrum was CAE: pass energy 150.0 eV. Atomic force microscopy (AFM, Dimension Edge, Bruker, USA) was used to analyze the size and shape of the prepared samples.

Cell culture

Mouse microglioma cell (GL261), mouse microglial cells (BV-2) and human glioma cells (U251) were purchased from the Cell Bank of the Chinese Academy of Sciences. These cells were grown in DMEM (Gibco, USA) medium with a high glucose content, 10% fetal bovine serum (Gibco, USA), and 1% penicillin plus streptomycin (Gibco, USA), all in a humidified environment of 5% CO_2 at 37 °C.

Biological activity of CDSBs

First, GL261 cells, U251 cells and BV-2 cells were counted and plates were seeded in 96-well plates (10^5 cells per well). CDSBs were decontaminated with 0.22 μm aqueous filter membrane, 200 μL of CDSBs prepared with DMEM at different concentrations were added and incubated for 24 h. CDs were also treated in this way. After washing twice with the PBS solution (HyClone, USA), 100 μL of 3-(4,5-dimethylthiazol-2-yl)-2,5-diphenyltetrazolium bromide (MTT, Solarbio, China) solution prepared with DMEM (1 mg mL^{-1}) were introduced and incubated for 4 h. The MTT solution were shaken off and 150 μL of dimethylsulfoxide (Macklin, China) were added to solubilize the formed formazan and placed on a shaker for 5 min. Finally, formazan absorbance was recorded at 490 nm using a Bio Tek microplate reader.

Apoptosis assay

The Annexin V-FITC/propidium iodide apoptosis kit (Elabscience, China) was applied to assess apoptosis. GL261 cells (5×10^5 cells per well) were treated with different doses of CDSBs (11, 22, 44 μg mL^{-1}) for 24 h. Subsequently, all cells were isolated using trypsinization without EDTA, and the apoptosis kit was employed to stain the cells in accordance with the manufacturer's instructions. A BD LSRFortessa flow cytometer (BD, USA) was used to capture all cell samples for flow cytometry. Data analysis was performed with FlowJo software.

Measurement of intracellular ROS production

GL261 cells were seeded in 6-well plates at a density of 5×10^5 cells per well. After overnight incubation, cells were treated with CDSBs with varying dose (11, 22, 44 μg mL^{-1}) for 24 h. Subsequently, cells were exposed to 10 μmol L^{-1} of DCFH-DA (Beyotime, China) for 20 min. The cells were then harvested and the fluorescence intensity was measured using a BD LSRFortessa flow cytometer (BD, USA).

Western blot analysis

GL261 cells were exposed to different doses of CDSBs (11, 22, 44 μg mL^{-1}) for 24 h. Subsequently, the cells were lysed in RIPA lysis buffer with added PMSF and protease/phosphatase inhibitor. The lysates were then separated by 12% SDS-polyacrylamide gel electrophoresis and transferred to polyvinylidene difluoride membranes (Millipore Sigma, USA). After blocking the membranes with 5% skim milk at room temperature for 1 h, primary antibodies were then incubated on the membranes overnight at 4 °C. Subsequently, the membranes were treated with secondary antibodies at room temperature for 1 h. The FluorChem M imaging system (ProteinSimple, USA) and the ProtoGlow ECL kit (National Diagnostics, USA) were applied to detect the immunoreactive bands. The antibodies used included the following. Bcl-2, Bax, Caspase-3, cleaved Caspase-3, PARP, cleaved PARP, NFκB, IκBα, phospho IκBα, and β-actin. All antibodies were obtained from Cell Signaling Technology (USA) and diluted 1 : 1000 before use.

Mitochondrial membrane potential assay

At a density of 5×10^5 cells per well, GL261 cells were placed in 6-well plates and left to grow overnight. The cells were then exposed to various doses of CDSBs (11, 22, 44 μg mL^{-1}) for 24 h. JC-1 (5 μg mL^{-1}) was subsequently added and allowed to incubate for 20 min. Cells were harvested and evaluated by flow cytometry and Leica SP8 laser confocal microscopy. The ratio of red/green fluorescence intensity was calculated by ImageJ software.

Cell TEM study

GL261 cells were seeded in 10 cm dishes (2×10^6 cells per dishes) by overnight culture. Then they were incubated with CDSBs (11, 22, 44 μg mL^{-1}) for 24 h. After that, cells were transferred to square carbon mesh, treated with 0.1 M cacodylate buffer containing 2.5% glutaraldehyde and 2% paraformaldehyde, and observed with a Hitachi TEM system (Hitachi, Japan).

Results and discussion

Characterizations of CDSBs

The TEM images of CDs and CDSBs are shown in Fig. 1. Fig. 1A and B show that the shapes of CDs and CDSBs are nearly spherical and well dispersed. The particle size of CDs ranges from 4.2 to 6.8 nm with a mean diameter of 5.8 nm (the lower right inset of Fig. 1A), while that of CDSBs varies from 1.7 to 3.3 nm with an average diameter of 2.23 nm (the lower right inset of Fig. 1B). HRTEM images identify a lattice spacing of

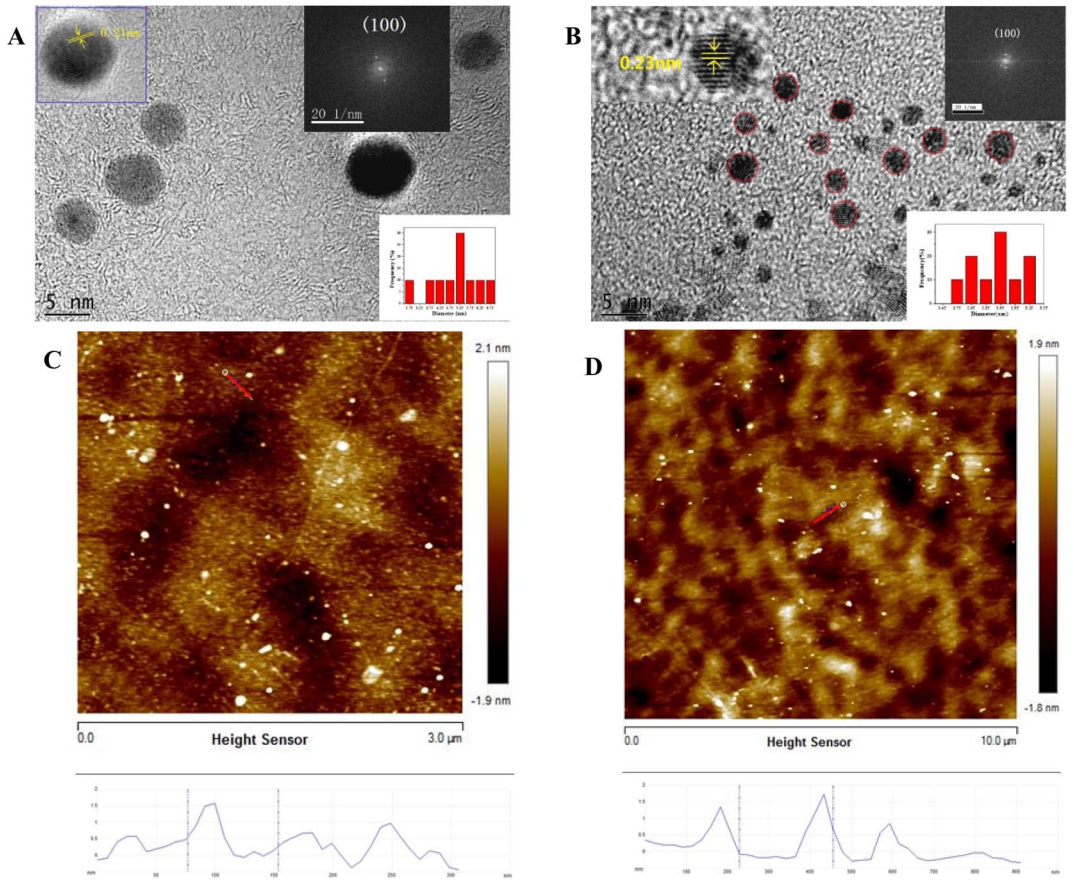

Fig. 1 TEM images of (A) CDs and (B) CDSBs, AFM images of (C) CDs and (D) CDSBs. The insets show HRTEM images, the size distributions, and FFT images.

0.21 nm for CDs (the upper inset of Fig. 1A) and 0.23 nm for CDSBs (the upper left inset of Fig. 1B). Fast Fourier transform (FFT) spot patterns indicate that the lattice spacings correspond to the (100) planes of graphite.[25] The AFM images show that the thickness of the CDs is about 1.6 nm (Fig. 1C), while that of the CDSBs is about 1.8 nm (Fig. 1D).

Fig. 2A shows the comparison of UV-Vis absorption spectra. It could be found that TPA has absorption peaks at 262 nm and 308 nm. The absorption peak located at 262 nm corresponds to π–π* electron transitions on the benzene ring, while the absorption peak at 308 nm is caused by n–π* electron transitions. CDs exhibit an absorption peak at 353 nm. CDSBs have an obvious characteristic peak of TPA at 262 nm, which means that CDs successfully combined with TPA. The absorption peak of CDSBs at 353 nm suggests that the main structure of CDs has not been destroyed. As shown in Fig. 2B, there is no obvious fluorescence emission peak for TPA. The emission peaks of CDs and CDSBs are significantly different. The emission peak of CDs is at 477 nm, and that of CDSBs is at 451 nm. TPA has electron-withdrawing groups that combine with lone pair electrons on CDs. This causes the fluorescence peak of CDSBs to shift blue. The benzene ring on TPA increases the overall conjugated system of CDSBs, leading to enhanced fluorescence. Therefore, the fluorescence intensity of CDSBs is much higher than that of CDs. Therefore, it could be preliminarily inferred that CDs were successfully combined with TPA.

The results of the Fourier transform infrared spectrum (FTIR) are shown in Fig. 2C. The broad characteristic peaks of CDs and CDSBs between 3500 and 3200 cm^{-1} include the stretching vibration of O–H and N–H. The characteristic peak of CDs at 1560 cm^{-1} belongs to N–H bending vibration of amines, while the same absorption peak of CDSBs decreases. CDSBs show a new characteristic peak at 1548 cm^{-1}, which corresponds to C=N stretching vibration.[26] CDs and CDSBs exhibit tensile and bending vibration peaks of C–H at 2940 cm^{-1} and 2870 cm^{-1}. CDSBs and CDs have C=O stretching vibration of the carboxyl group at 1656 cm^{-1}. The characteristic peak of CDSBs at 1696 cm^{-1} is the C=O stretching vibration absorption peak in the aldehyde group of TPA. The characteristic peaks of CDs and CDSBs at 1108 cm^{-1} are attributed to C–N/C–O stretching vibrations. The results show that the prepared CDs have amino groups (–NH_2) and carboxyl groups (–COOH), and the existence of C=N also proves the successful preparation of CDSBs.

The full XPS spectra (Fig. 3A and B) confirm that CDs and CDSBs both have three representative peaks of C 1s, N 1s, and O 1s. For CDs, the relative elemental contents are about 75.00% (C), 12.66% (N) and 12.34% (O), but for CDSBs, there are 75.43% (C), 12.34% (N), and 12.23% (O), respectively. The increase in the relative elemental contents of C is attributed to the combination of TPA. In the C 1s spectrum of CDs (Fig. 3C), three peaks can be observed at 284.8 eV (C–C/C=C), 286.0 eV (C–N/C–O)

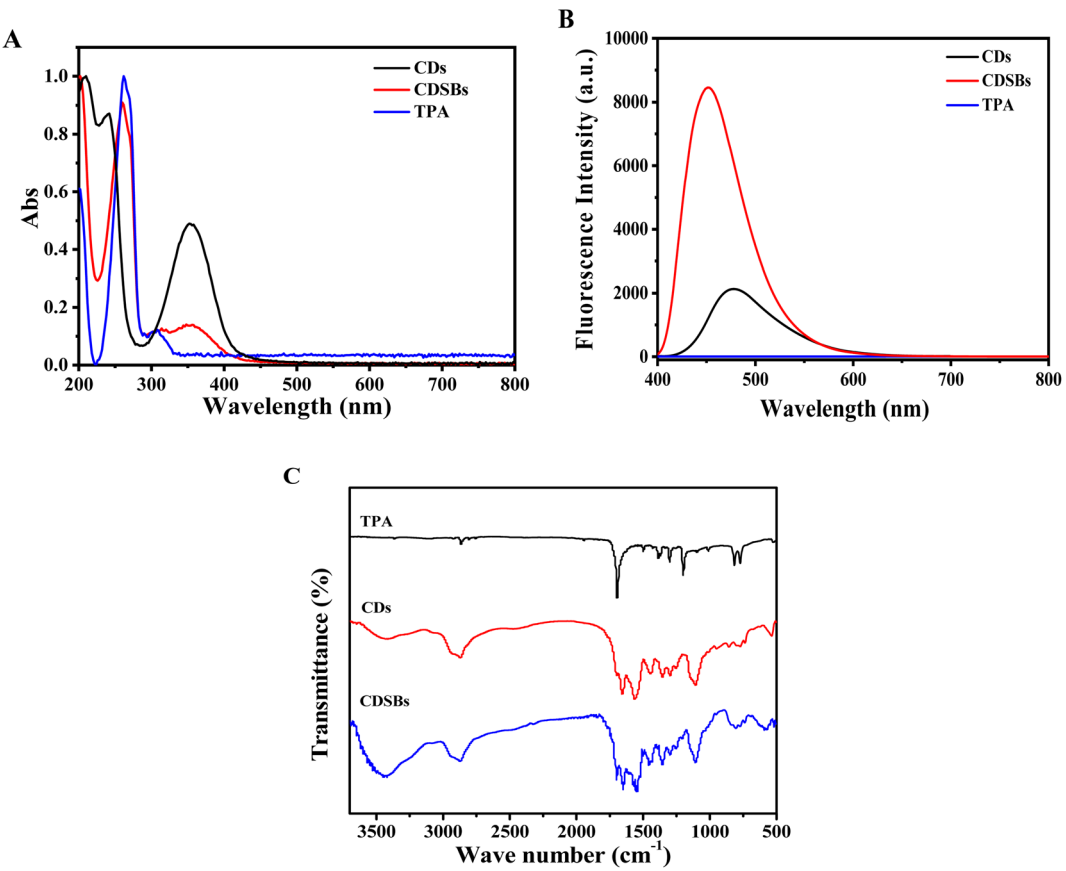

Fig. 2 (A) UV-Vis absorption spectra, (B) fluorescence spectra, (C) FTIR of CDs, CDSBs and TPA.

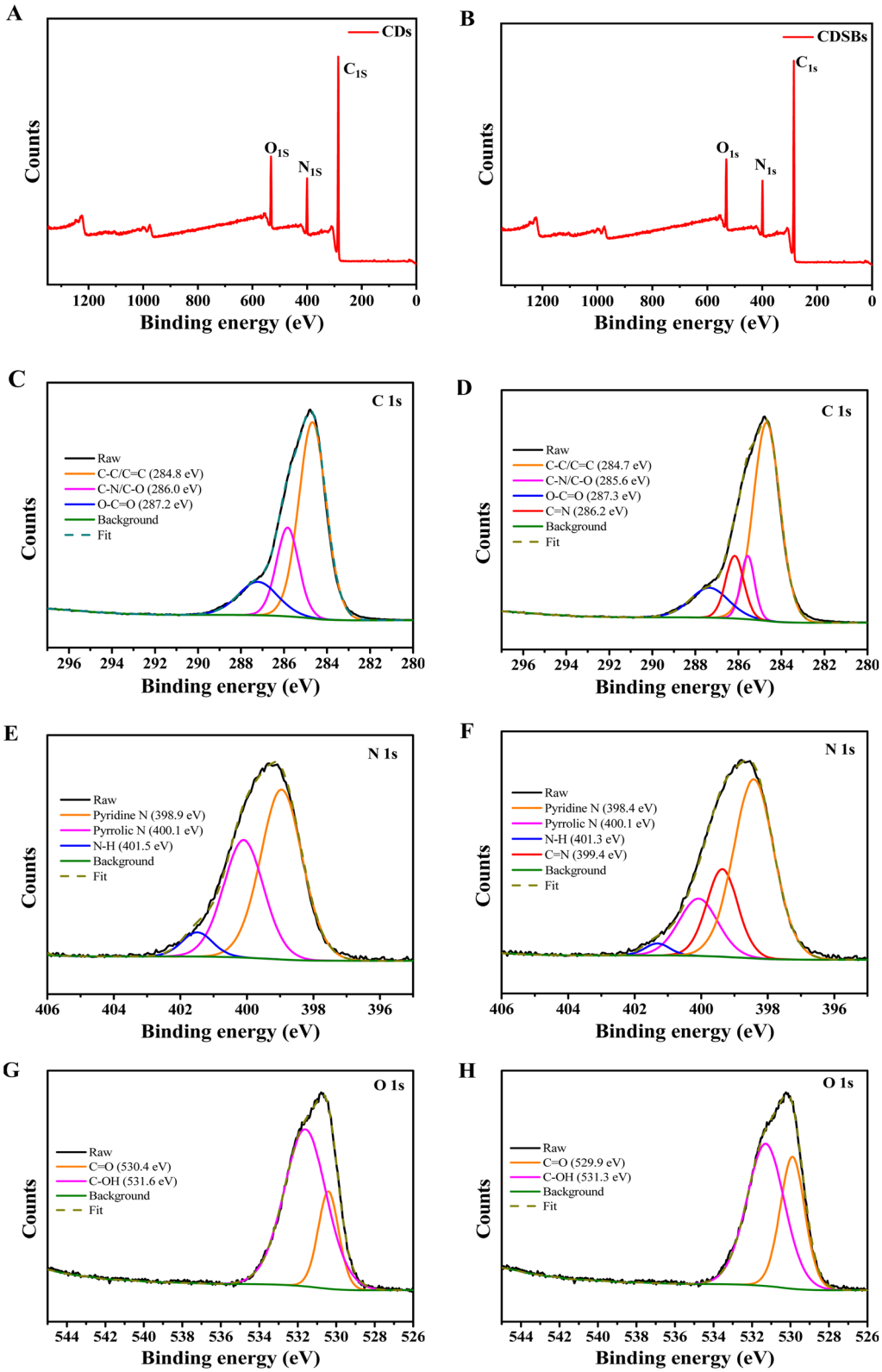

Fig. 3 Full XPS spectra of (A) CDs and (B) CDSBs, C 1s XPS spectra of (C) CDs and (D) CDSBs, N 1s XPS spectra of (E) CDs and (F) CDSBs, O 1s XPS spectra of (G) CDs and (H) CDSBs.

and 287.2 eV (O–C=O). The three peaks at 398.9 eV, 400.1 eV and 401.5 eV in the N 1s spectrum of CDs point to pyridine N, pyrrolic N and N–H, respectively (Fig. 3E). In the O 1s spectrum, the CDs peaks can be observed at 530.4 eV (C=O) and 531.6 eV (C–OH) (Fig. 3G).[27] On the basis of the XPS spectra of CDs, it indicates that CDs have abundant hydrophilic groups (–NH_2

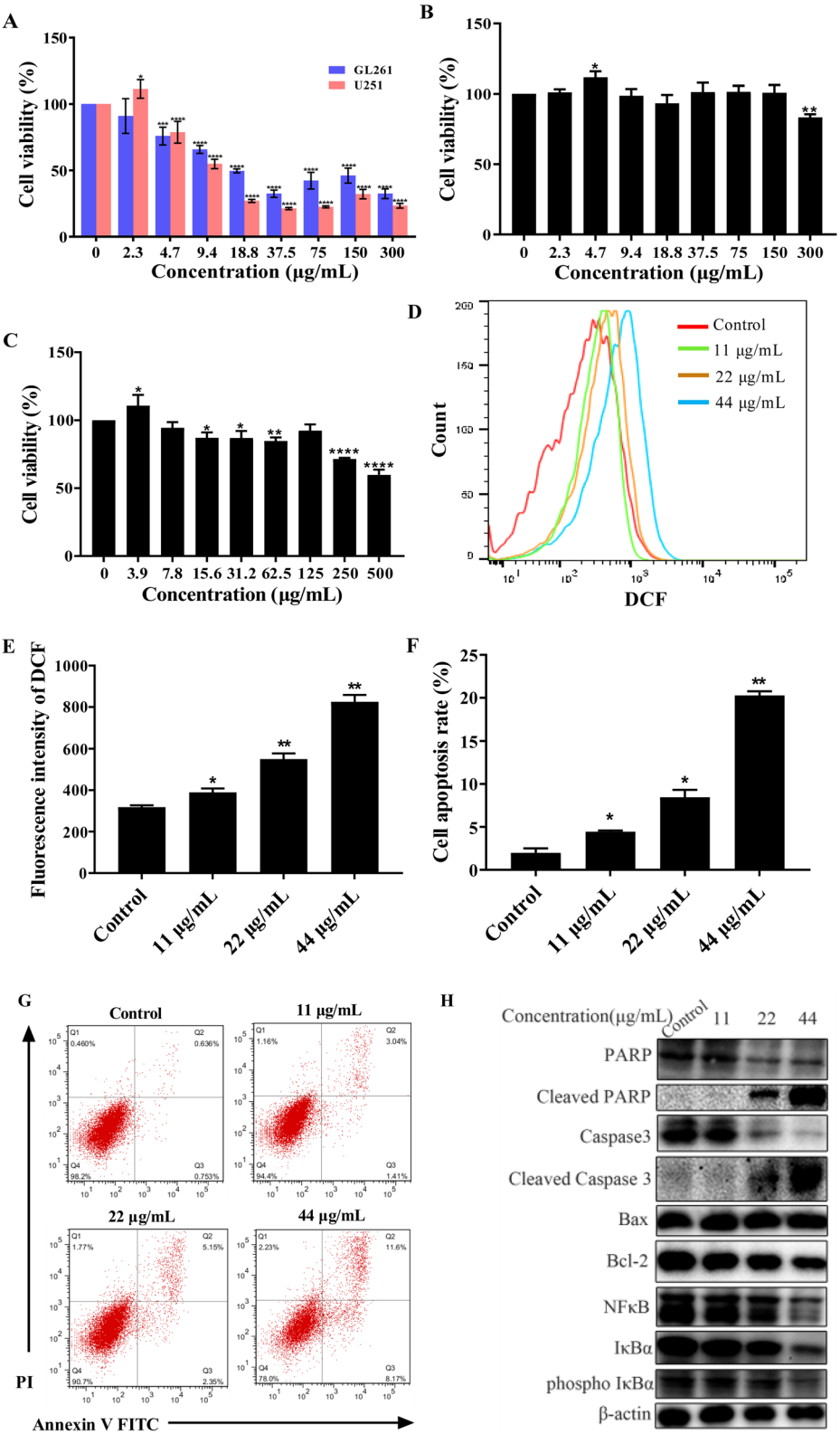

Fig. 4 (A) Results of the MTT test for CDSBs in GL261 cells and U251 cells. (B) Results of the CDs MTT test in GL261 cells. (C) MTT results of CDSBs in BV-2 cells. (D) ROS levels in GL261 cells with DCF as an indicator. (E) The fluorescence intensity of DCF. (F) The rate of quantitative cell apoptosis. (G) Cell apoptosis analyzed by flow cytometry. (H) The expression of apoptosis-related proteins in GL261 cells. Data were presented as mean ± standard deviation (SD). *$p < 0.05$, **$p < 0.01$, ***$p < 0.001$, ****$p < 0.0001$ *versus* control (without treated CDSBs).

and –COOH). The peak positions of CDSBs C 1s and N 1s are similar to those of CDs, with a more peak at 286.2 eV (C═N) for C 1s (Fig. 3D) and a more peak at 399.4 eV (C═N) for N 1s (Fig. 3F).[28] This means that $-NH_2$ on CDs was successfully combined with the carbonyl group on TPA to form an imino group. Additionally, compared to the O 1s peaks of CDs, the peak corresponding to C═O of CDSBs is significantly enhanced, attributed to the combination between CDs and TPA (Fig. 3H).

Biological activity of CDSBs

To test the anticancer activity of CDSBs, we used MTT to carry out the cytotoxicity test. First, we detected the MTT of GL261 and U251 cells. The results are shown in Fig. 4A. CDSBs have good anticancer effects on GL261 and U251 cells with IC_{50} values of 17.9 μg mL^{-1} and 14.9 μg mL^{-1}, respectively. Based on previous reports, BP-1-102 had been confirmed to be an inhibitor of signal transducer and transcription 3 (STAT3) activator.[29] BP-1-102 had an IC_{50} of 10.51 μM (6.59 μg mL^{-1}), which

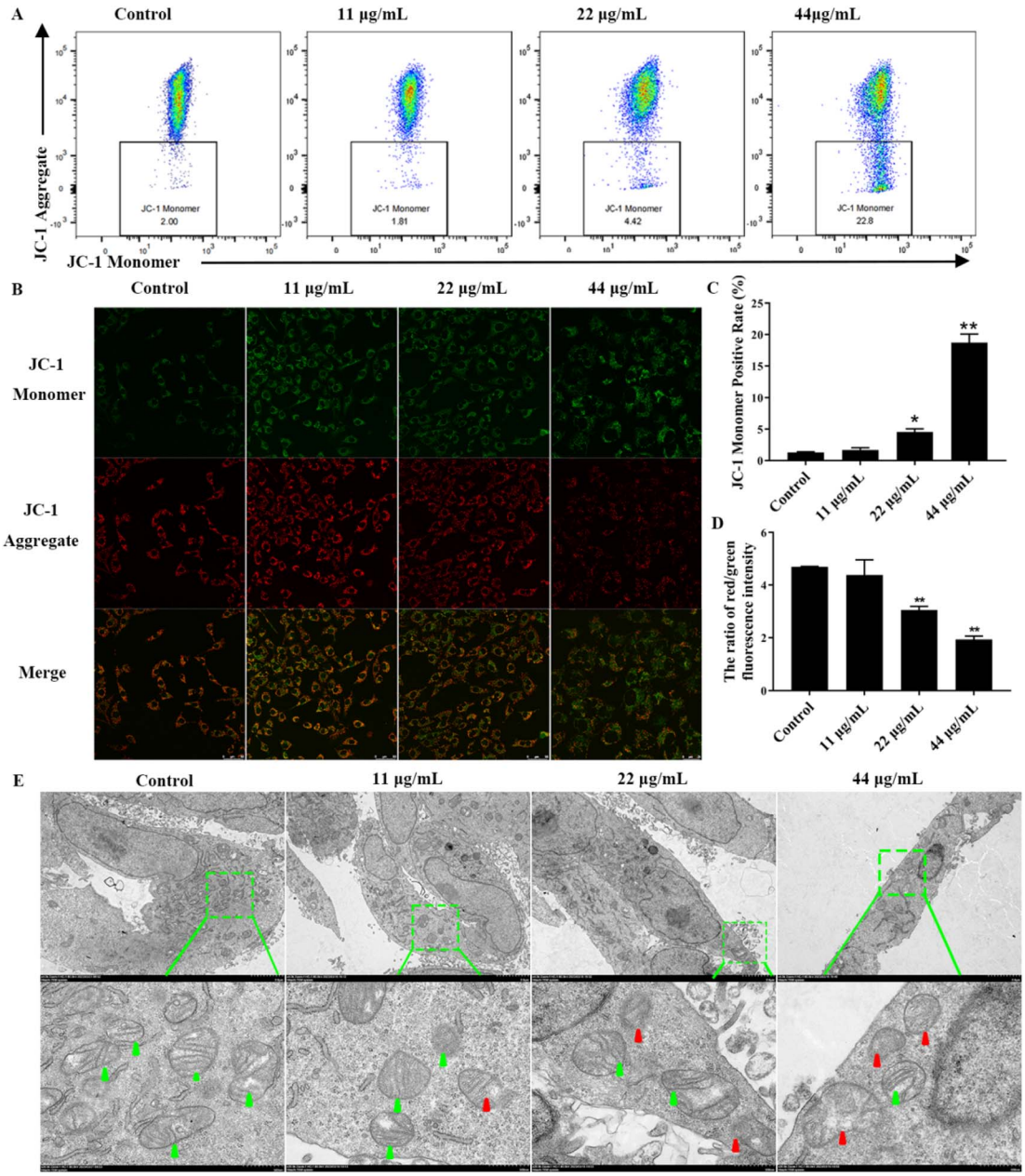

Fig. 5 CDSBs-induced mitochondrial damage. (A) Mitochondrial membrane potential detected by flow cytometry, which was stained with JC-1. (B) Mitochondrial membrane potential detected by confocal laser microscopy. Red fluorescence indicated aggregates, and green fluorescence indicated monomers. (C) The percentage of JC-1 monomer-positive cells. (D) The red-to-green fluorescence ratio of cells was quantified. (E) Representative TEM images showing morphological changes in mitochondria in GL261 cells. Green and red arrows indicated normal and damaged mitochondria, respectively. The scale bars were 2 μm (upper panel) and 500 nm (lower panel). Data were presented as mean ± standard deviation (SD). *$p < 0.05$, **$p < 0.01$ *versus* control.

prevented U251 cells from proliferating. The IC_{50} of the cisplatin complex against GL261 synthesized by Mao *et al.* was 17.4 μM (14 μg mL^{-1}).[30] It is similar to the IC_{50} of CDSBs against GL261, indicating that the anticancer effect of CDSBs is equivalent to it. While the toxicity of CDSBs (IC_{50} > 500 μg mL^{-1}) to normal cells is much less than that of cisplatin complexes (IC_{50} = 45.0 μg mL^{-1}), which implies CDSBs have better biological safety. However, CDSBs exhibit low toxicity on HeLa cells (Fig. S1†). Then we also studied the anticancer activity of CDs in GL261 cells. As shown in Fig. 4B, CDs have low toxicity with GL261, with cell viability above 80% at a concentration of 300 μg mL^{-1}. The results confirm that CDs are less toxic to cancer cells, while CDSBs have anticancer properties. Finally, we also investigated the toxicity of CDSBs in the normal cell line BV-2. The results are shown in Fig. 4C. CDSBs have lower toxicity to BV-2 cells (cell viability higher than 85%) at action concentration. Therefore, CDSBs have good cell selectivity with little killing effect on normal cells at effective concentrations against cancer cells.

The mechanism of apoptosis

Most chemotherapeutic agents can cause elevated ROS levels in tumor cells, which can induce apoptosis through endogenous and exogenous pathways. 2′,7′-dichlorofluorescein diacetate (DCF) was used as a fluorescent sensor to measure ROS levels in GL261 cancer cells treated with CDSBs. After exposure to different doses of CDSBs, a concentration of 44 μg mL^{-1} resulted in approximately 13 times higher intracellular ROS production than the control group (Fig. 4D and E). The significant increase in intracellular ROS production demonstrates that mitochondria-targeted CDSBs have the potential to induce a localized ROS surge by disrupting mitochondrial homeostasis.[31]

Double staining with Annexin V FITC and propidium iodide was used to examine the total population of apoptotic cells. The results show that the apoptosis rate increases with increasing CDSBs concentration (Fig. 4F and G). Western blot analysis of apoptosis-related proteins reveals that CDSBs (44 μg mL^{-1}) can significantly down-regulate Bax, Bcl-2, caspase 3, and PARP, while increasing cleaved caspase 3 and cleaved PARP in GL261 cells (Fig. 4H). NFκB is also an inhibitor of apoptosis. Western blot analysis also demonstrates that CDSBs (44 μg mL^{-1}) inhibit the expression of NFκB-related protein, including NFκB, IκBα and phospho IκBα (Fig. 4H). These findings fully demonstrate the potent pro-apoptotic effect of CDSBs.

Reduced mitochondrial membrane potential and subsequent mitochondrial damage can induce apoptosis. Therefore, we explored the effects of upstream mitochondrial damage of apoptotic after CDSBs treatment. First, to gain a deeper understanding of the mitochondrial damage caused by CDSBs, we used the indicator dye JC-1 to determine the mitochondrial membrane potential ($\Delta\Psi_m$). JC-1 formed J-aggregates in cells with high mitochondrial membrane potential and emitted red fluorescence, while it remained monomeric in cells with low mitochondrial membrane potential and emitted green fluorescence. Flow cytometry analysis shows that mitochondrial membrane potential decreases with increasing CDSBs concentration, as evidenced by the enhanced green fluorescence of cells, indicating severe loss of mitochondrial membrane potential (Fig. 5A and C). The fluorescence imaging results are consistent with the flow cytometry data (Fig. 5B and D).

To further examine the morphological variations induced by CDSBs treatment, we used TEM to examine mitochondrial structure. As shown in Fig. 5E, control group cells display healthy mitochondria with typical tubular cristae and crista junctions. However, with increasing concentration of CDSBs, the morphological changes in mitochondria became more pronounced. Cells treated with high concentrations of CDSBs exhibit severe mitochondrial damage, characterized by severe crista breakage and abnormal vacuoles. These findings suggest that CDSBs have a detrimental effect on mitochondria, which serve as essential energy sources for cells. Therefore, CDSBs-induced mitochondrial damage can be a fatal blow to cancer cells. Taken together, these results validate that CDSBs could potentially induce mitochondrial disruption and eventually lead to cancer cells apoptosis.

From the above work, CDSBs are known to promote GL261 cells apoptosis. Under the action of CDSBs, the mitochondria of GL261 cells are damaged and the intracellular protein content is altered, leading to a decrease in mitochondrial membrane potential and the production of large amounts of ROS, resulting in apoptosis (Fig. 6). During this process, the level of Bcl-2 decreases, thus reducing its inhibitory effect on cell apoptosis. The decrease in IκBα and subsequent NFκB levels weakens their inhibitions on caspase 3 and apoptosis. The increased content of cleaved caspase 3 indicates that it plays an important role in the apoptosis of GL261 cells, and the increase in cleaved PARP demonstrates the successful activation of caspase 3.

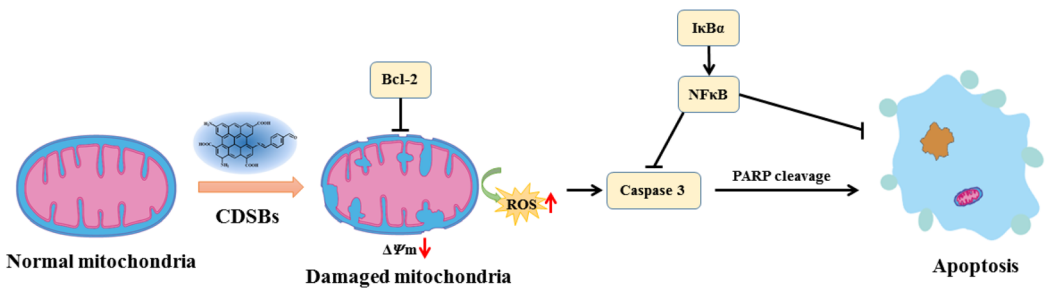

Fig. 6 The apoptosis mechanism of GL261 cells.

Conclusions

In this work, CDs containing amino groups on the surface were synthesized by the hydrothermal method, and then CDs and TPA were condensed to form CDSBs. According to the results of the cytotoxicity assays, it could be seen that CDSBs have an inhibitory effect on GL261 and U251 cells. Moreover, CDSBs perform good biocompatibility in normal glial BV-2 cells. The results of apoptosis and ROS production show that CDSBs induce GL261 cells to produce more ROS for apoptosis. From the results of mitochondrial membrane potential and mitochondrial structure studies, the mitochondrial membrane potential of GL261 cells is reduced and the morphology is impaired by CDSBs. These results show that CDSBs have an anticancer effect on glioma cells and provide a new material for anticancer.

Conflicts of interest

There are no conflicts to declare.

Acknowledgements

The authors gratefully acknowledge the financial support from Foundation of NHC Key Laboratory of Technical Evaluation of Fertility Regulation for Non-Human Primate, Fujian Maternity and Child Health Hospital (2022-NHP-01), Joint Funds for the Innovation of Science and Technology, Fujian Province (2021Y9184), Natural Science Foundation of Fujian Province (2019J01300).

References

1 Y. Zhou, C. Fang, H. Xu, *et al.*, Ferroptosis in glioma treatment: Current situation, prospects and drug applications, *Front. Oncol.*, 2022, **12**, 5328.
2 M. Llaguno-Munive, M. I. Vazquez-Lopez, R. Jurado, *et al.*, Mifepristone repurposing in treatment of high-grade gliomas, *Front. Oncol.*, 2022, **11**, 606907.
3 F. Tong, J. Zhao, Z. Fang, *et al.*, MUC1 promotes glioblastoma progression and TMZ resistance by stabilizing EGFRvIII, *Pharmacol. Res.*, 2023, **187**, 106606.
4 M. N. Ahamad, K. Iman, M. K. Raza, *et al.*, Anticancer properties, apoptosis and catecholase mimic activities of dinuclear cobalt (II) and copper (II) Schiff base complexes, *Bioorg. Chem.*, 2020, **95**, 103561.
5 A. Soroceanu and A. Bargan, Advanced and biomedical applications of Schiff-base ligands and their metal complexes: A review, *Crystals*, 2022, **12**, 1436.
6 Y. Mi, Y. Chen, W. Tan, *et al.*, The influence of bioactive glyoxylate bearing Schiff base on antifungal and antioxidant activities to chitosan quaternary ammonium salts, *Carbohydr. Polym.*, 2022, **278**, 118970.
7 L. Xu, Q. Meng, Z. Zhang, *et al.*, Chitosan-salicylide Schiff base with aggregation-induced emission property and its multiple applications, *Int. J. Biol. Macromol.*, 2022, **209**, 1124–1132.
8 M. A. Ali, K. A. Aswathy, G. Munuswamy-Ramanujam, *et al.*, Pyridine and isoxazole substituted 3-formylindole-based chitosan Schiff base polymer: antimicrobial, antioxidant and in vitro cytotoxicity studies on THP-1 cells, *Int. J. Biol. Macromol.*, 2023, **225**, 1575–1587.
9 A. Nemat, I. N. Khan, S. Kalsoom, *et al.*, Synthesis, anticancer evaluation and molecular docking studies of methotrexate's novel Schiff base derivatives against malignant glioma cell lines, *J. Biomol. Struct. Dyn.*, 2022, **40**, 2865–2877.
10 S. Chen, X. Liu, X. Ge, *et al.*, Lysosome-targeted iridium (III) compounds with pyridine-triphenylamine Schiff base ligands: syntheses, antitumor applications and mechanisms, *Inorg. Chem. Front.*, 2020, **7**, 91–100.
11 C. Shiju, D. Arish and S. Kumaresan, Novel water soluble Schiff base metal complexes: synthesis, characterization, antimicrobial-, DNA cleavage, and anticancer activity, *J. Mol. Struct.*, 2020, **1221**, 128770.
12 S. Feizpour, S. A. Hosseini-Yazdi, F. Safarzadeh, *et al.*, A novel water-soluble thiosemicarbazone Schiff base ligand and its complexes as potential anticancer agents and cellular fluorescence imaging, *JBIC, J. Biol. Inorg. Chem.*, 2023, **28**, 457–472.
13 B. Shi, H. Zhang, Z. Shen, *et al.*, Developing a chitosan supported imidazole Schiff-base for high-efficiency gene delivery, *Polym. Chem.*, 2013, **4**, 840–850.
14 M. S. S. Adam, M. M. Makhlouf, F. Ullah, *et al.*, Catalytic and biological reactivities of mononuclear copper (II) and vanadyl (II) complexes of naphthalenylimino-phenolate sodium sulfonate, *J. Taiwan Inst. Chem. Eng.*, 2021, **118**, 12–28.
15 B. Biswas, P. Choudhury, A. Ghosh, *et al.*, A water soluble Ni-Schiff base complex for homogeneous green catalytic C-S cross-coupling reactions, *Inorg. Chim. Acta*, 2021, **532**, 120755.
16 S. Xue, P. Li, L. Sun, *et al.*, The formation process and mechanism of carbon dots prepared from aromatic compounds as precursors: a review, *Small*, 2023, **19**, 2206180.
17 A. Döring, E. Ushakova and A. L. Rogach, Chiral carbon dots: synthesis, optical properties, and emerging applications, *Light: Sci. Appl.*, 2022, **11**, 75.
18 Y. Park, Y. Kim, H. Chang, *et al.*, Biocompatible nitrogen-doped carbon dots: synthesis, characterization, and application, *J. Mater. Chem. B*, 2020, **8**, 8935–8951.
19 B. P. Frank, L. R. Sigmon, A. R. Deline, *et al.*, Photochemical transformations of carbon dots in aqueous environments, *Environ. Sci. Technol.*, 2020, **54**, 4160–4170.
20 X. P. Chen, Y. F. Zhuang, J. Chen, *et al.*, Novel ratiometric fluorescence and colorimetric dual-mode biosensors for Cu^{2+} and biothiols detection based on norepinephrine modified carbon dots, *Microchem. J.*, 2022, **181**, 107828.
21 S. Bayda, E. Amadio, S. Cailotto, *et al.*, Carbon dots for cancer nanomedicine: a bright future, *Nanoscale Adv.*, 2021, **3**, 5183–5221.
22 B. Han, L. Shen, H. Xie, *et al.*, Synthesis of carbon dots with hemostatic effects using traditional Chinese medicine as a biomass carbon source, *ACS Omega*, 2023, **8**, 3176–3183.

23 X. Jia, M. Pei, X. Zhao, *et al.*, PEGylated oxidized alginate-DOX prodrug conjugate nanoparticles cross-linked with fluorescent carbon dots for tumor theranostics, *ACS Biomater. Sci. Eng.*, 2016, **2**, 1641–1648.
24 C. Lian, J. Zhang, B. Ruan, *et al.*, Near infrared light-actuated PEG wrapping carbon nanodots loaded cisplatin for targeted therapy of lung cancer therapy, *J. Cluster Sci.*, 2021, **32**, 125–133.
25 J. Xu, Y. Wang, L. Sun, *et al.*, Chitosan and κ-carrageenan-derived nitrogen and sulfur co-doped carbon dots "on-off-on" fluorescent probe for sequential detection of Fe^{3+} and ascorbic acid, *Int. J. Biol. Macromol.*, 2021, **191**, 1221–1227.
26 J. Song, S. Chen, Q. Zhang, *et al.*, Preparation and characterization of the bonding performance of a starch-based water resistance adhesive by Schiff base reaction, *Int. J. Biol. Macromol.*, 2023, **251**, 126254.
27 S. Tang, D. Chen, Y. Yang, *et al.*, Mechanisms behind multicolor tunable near-infrared triple emission in graphene quantum dots and ratio fluorescent probe for water detection, *J. Colloid Interface Sci.*, 2022, **617**, 182–192.
28 N. Z. N. Hashim, K. Kassim, H. M. Zaki, *et al.*, XPS and DFT investigations of corrosion inhibition of substituted benzylidene Schiff bases on mild steel in hydrochloric acid, *Appl. Surf. Sci.*, 2019, **476**, 861–877.
29 C. Zhang, T. Wu, L. Guan, *et al.*, Effects of STAT3 inhibitor BP-1-102 on the proliferation, invasiveness, apoptosis and neurosphere formation of glioma cells in vitro, *Cell Biochem. Biophys.*, 2022, **80**, 723–735.
30 X. Mao, S. Wu, P. Calero-Pérez, *et al.*, Synthesis and validation of a bioinspired catechol-functionalized Pt (IV) prodrug for preclinical intranasal glioblastoma treatment, *Cancers*, 2022, **14**, 410.
31 K. Lin, Z. Ma, J. Li, *et al.*, Single small molecule-assembled mitochondria targeting nanofibers for enhanced photodynamic cancer therapy in vivo, *Adv. Funct. Mater.*, 2021, **31**, 2008460.